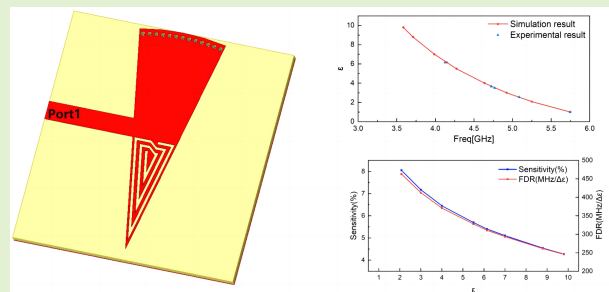


A Sixteenth-Mode Substrate Integrated Waveguide Sensor Loaded With CCRR Resonator Used for Solid Permittivity Measurement

Wudi Ji¹ and Guohua Liu¹, *Member, IEEE*

Abstract—In this article, we propose a sixteenth-mode substrate integrated waveguide (SMSIW) planar microwave resonant sensor for solid permittivity measurement. The sensor incorporates a complementary curved ring resonator (CCRR) structure strategically positioned within the SMSIW cavity, where the electric field is most concentrated, effectively enhancing sensor performance. By loading material under test (MUT) onto the CCRR resonator, the electric field distribution around the sensor will be changed, resulting in a change in the resonant frequency of the sensor, which makes the sensor be able to measure permittivity of different solid materials efficiently. The article comprehensively analyzes the equivalent model of the sensor and conducts electromagnetic simulation experiments to validate its performance. In addition, the sensor's performance is evaluated through experiments involving four different materials under test with dimensions of $10 \times 10 \times 0.762$ mm. Experimental results show that the performance of the proposed sensor significantly improved, with an average sensitivity of 6.585%, an average resolution of 378.46 MHz/ $\Delta\epsilon$, and an impressively low error rate of only 0.7845%. The compact size with $21 \times 20 \times 0.762$ mm of the sensor is in line with the trend of sensor miniaturization.

Index Terms—Complementary curved ring resonator (CCRR), high sensitivity, low error rate, sixteenth-mode substrate integrated waveguide (SMSIW), small size.



I. INTRODUCTION

IN RECENT years, microwave measurement technology has been widely applied in various fields due to its miniaturization, low cost, and real-time characteristics. Microwave sensors have important applications in agriculture, biology [1], [2], [3], and industry [4]. Many microwave planar sensors for measuring material permittivities have been proposed. Planar microwave sensors can be classified according to various criteria. They can be divided into coupling-modulation sensors [5], [6], phase-variation sensors [7], frequency-splitting sensors [8], and frequency-conversion sensors [9]. A differential microwave permittivity sensor based on the reflection coefficient of microstrip lines terminated with series LC resonators

was proposed by Ebrahimi et al. [6], and the experiment results proved that differential sensing plays an important role in removing cross-sensitivity and improving sensor measurement accuracy. A low-cost and portable phase-variation planar microwave sensor operating in reflective mode was presented by Vélez [7]; the sensor replaces the vector network analyzer (VNA) with a microcontroller, a voltage-controlled oscillator (VCO), a digital-to-analog converter (DAC), and an RF/microwave gain/phase detector, reducing cost without sacrificing sensor performance. It is mentioned that the reflection mode phase change sensor has significant advantages and high performance (mainly high sensitivity). An embroidered textile frequency-splitting microwave sensor based on a pair of identical stepped-impedance resonators (SIRs) loading a microstrip transmission line was proposed by Vélez [8]. The presented textile frequency-splitting microwave sensor exhibits the following advantages: mainly high sensitivity and resolution, good dynamic range, easy fabrication process, and wearability. A microwave measurement system for complex permittivity of liquid samples based on improved half-mode substrate integrated waveguide (HMSIW) was proposed by Wu

Manuscript received 2 April 2024; revised 6 June 2024; accepted 6 June 2024. Date of publication 21 June 2024; date of current version 1 August 2024. The associate editor coordinating the review of this article and approving it for publication was Dr. Shyqri Haxha. (Corresponding author: Guohua Liu.)

The authors are with the School of Electronics and Information Engineering, Hangzhou Dianzi University, Hangzhou 310018, China (e-mail: 21041314@hdu.edu.cn; ghliu@hdu.edu.cn).

Digital Object Identifier 10.1109/JSEN.2024.3412072

and Zhao [9]. It combines passive resonant sensors with RF circuits, eliminating the dependence on expensive VNA and reducing costs. However, it suffers from large errors due to the absence of VNA. A complementary split-ring resonator (CSRR)-based antenna sensor for full characterization of magneto-dielectric materials was proposed by Zhang et al. [10]. The sensor measures through two complementary resonance peaks, expanding the measurement range of complex permittivities and permeability. However, experimental data indicate insufficient sensitivity. A planar microwave sensor loaded with complementary curved ring resonators (CCRRs) for measuring permittivity of substrate materials was proposed by Han et al. [11]. The experimental results demonstrate that the sensor features high sensitivity, high resolution, and high measurement accuracy. However, shrinking the size of the sensor is challenging due to the use of full-mode substrate integrated waveguides (FMSIW). To address this problem, it introduced a quarter-mode substrate integrated waveguide (QMSIW) microwave resonant sensor loaded with a structure of CCRR in [12]. Due to the use of QMSIW, the sensor's size is significantly reduced while maintaining high sensitivity, high resolution, and low error. However, there is still considerable room for improvement in terms of structure and application. This inspires us to explore whether it is possible to further miniaturize the substrate integrated waveguide (SIW) sensor without sacrificing sensitivity and resolution.

Currently, electronic devices are rapidly advancing toward miniaturization and integration. SIW as a planar structure combines the characteristics of microstrip and rectangular waveguides. It is widely used in various microwave device designs due to its compact structure, versatility, high integration, low insertion loss, and high power-handling capabilities [13], [14], [15], [16] [17], [18], [19]. A modified SIW re-entrant microwave sensor was proposed by Chen et al. [20], which can be used to measure the complex permittivity of liquids. The QMSIW microwave resonant sensor proposed by Qi et al. [12] reduces the volume by 25% compared with FMSIW. Models of FMSIW, HMSIW, QMSIW, eighth-mode SIW (EMSIW), and sixteenth-mode SIW (SMSIW) were introduced in [21], [22], [23], and [24]. The application of QMSIW, EMSIW, and SMSIW in filter design inspires us to apply the design ideas of SMSIW to microwave planar resonant sensors.

Microwave planar sensors typically use structures such as split-ring resonator (SRR) [25], [26] [5], [27], [28], [29], CSRR [10], [30], [31], [32] [4], [33], [34], and the loaded CCRR structure [11], [12]. A microwave sensor using a pair of SRRs was proposed by Ebrahimi et al. [5]; the sensor improved the robustness to environmental factors producing cross-sensitivity or miscalibration by loading a pair of identical SRRs on both sides of the microstrip line and using one of them as a differential measurement reference. However, because the SRR structure must be in the same plane as the microstrip line, its sensors are difficult to miniaturize and highly integrate. As a new type of sensor resonant structure, CSRR is renowned for its unique resonant structure and its excellent performance, and it is widely used in various

microwave fields, including antennas, sensors, and filters. Compared with the SRR structure, the CSRR structure does not need to be in the same plane as the microstrip line but is etched on the ground surface of the sensor, making the sensor more compact in size. A novel sensor known as the planar microstrip-based triple-ring bridge (TRB)-CSRR sensor was introduced by Singh et al. [1]; the sensor improves its sensitivity to dielectric properties by amplifying its ability to precisely limit the electric field at the resonant frequency. A new design of teeth gear-circular substrate integrated waveguide (TG-CSIW) sensor to extract complex permittivity of liquids was suggested by Rahman et al. [35]; the introduction of the angle between the input and output ports (ABIOP) not only reduces the size of the sensor but also increases the unloaded quality factor to 700. The CCRR structure is evolved from the basic CSRR structure. A comparison of the electric field distribution between the CSRR and CCRR structures under the same conditions shows that the electric field distribution of CCRR is denser. CCRR and CSRR are compared in [11]; the experiments compared the structures of CCRR and CSRR and the influence of different ring numbers on the electric field intensity. The experimental data showed that compared with CSRR, CCRR has a higher electric field intensity at the resonant frequency. The electric field intensity increases with the number of rings. Inspired by these studies, we etch the CCRR structure onto the surface of the SMSIW. While maintaining sensor sensitivity (6.585%), the sensor's size is significantly reduced to 21×20 mm, and it still has extremely high resolution.

In this article, a novel sensor that incorporates the CCRR structure onto the surface of the SMSIW is proposed. Compared with the FMSIW, its size occupies only 6.25% [36]. The CCRR is etched in the area of highest electric field concentration within the SMSIW cavity. When the material under test (MUT) is loaded above the CCRR resonator, the electric field distribution around the sensor will be changed, resulting in a change in the resonant frequency of the sensor, which makes the sensor to measure permittivity of different solid materials efficiently. The performance of the proposed sensor is significantly improved, with an average sensitivity of 6.585%, an average resolution of 378.46 MHz/ $\Delta\epsilon$, and an impressively low error rate of only 0.7845%.

This article is organized as follows. Section II presents the operation principle of the CCRR-SMSIW sensor. Section III introduces the design of CCRR-SMSIW sensor and analysis of the equivalent circuit and sensitivity. Section IV exhibits the experimental results of the proposed sensor, then followed by a conclusion in Section V.

II. OPERATION PRINCIPLE

The microwave resonant sensor uses the interaction between microwaves and the target object to detect information about the target object by measuring the changes in resonant frequency. When the target object interacts with microwaves, the electric and magnetic fields around the sensor are disturbed, causing a variation in the resonant frequency of the

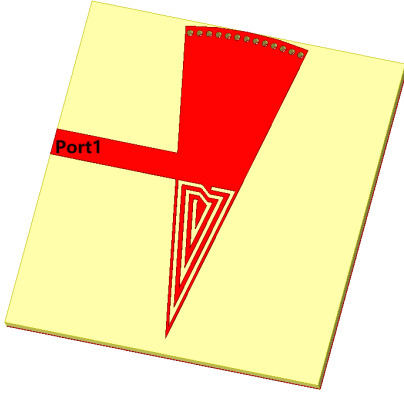


Fig. 1. Three-dimensional image of the SMSIW-CCRR sensor.

sensor [37]. The change in resonant frequency is given by the following equation:

$$\frac{\Delta f_r}{f_r} = \frac{\int_v (\Delta \varepsilon E_1 \cdot E_0 + \Delta \mu H_1 \cdot H_0) dv}{\int_v (\varepsilon_0 |E_0|^2 + \mu_0 |H_0|^2) dv} \quad (1)$$

where f_r is the resonant frequency when the sensor is without loading any material, Δf_r represents the offset of sensor's resonant frequency when it is loaded with a material, and v denotes the volume of the target object. ε_0 and μ_0 are the permittivity and permeability values of free space, respectively. $\Delta \varepsilon$ and $\Delta \mu$ represent the changes in permittivity and permeability between target object and free space, respectively. E_0 and H_0 denote the electric field and magnetic field under unloaded conditions, respectively, while E_1 and H_1 mean the electric field and magnetic field under loaded conditions, respectively.

According to the description in [23], the permeability of small-sized solid materials is essentially the same as that of free space, which means $\Delta \mu = 0$. When the circuit is resonant, the electric field energy stored in the circuit equals the magnetic field energy. Therefore, (1) can be transformed into

$$\frac{\Delta f_r}{f_r} = \frac{\int_{v_{\text{mut}}} (\Delta \varepsilon E_1 \cdot E_0) dv}{2 \int_v \varepsilon_0 |E_0|^2 dv}. \quad (2)$$

In the provided equation, v_{mut} signifies the volume of the MUT. As elucidated by (2), when the sensor loads the MUT, its resonant frequency will be shifted. Consequently, this alteration in resonant frequency can be detected through a VNA, which can be used to deduce the MUT's permittivity. It is worth noting that since it assumes that the perturbed object is an ideal lossless medium, the permittivity value obtained by (1) and (2) is the real part of the permittivity without the imaginary part value.

III. DESIGN AND ANALYSIS

The proposed sensor incorporates the CCRR structure onto the surface of the SMSIW as depicted in Fig. 1. The curved surface of the SMSIW is connected to the top metal layer via holes, thus establishing the open side as a quasi-magnetic wall and the closed side as an electric wall. According to the operational principles of waveguides [36], the main mode

of SMSIW is TM_{010} mode. When the fan-shaped SMSIW operates in TM_{010} mode, the electric field attains its maximum value at the center of the sector. Studies have revealed that field strength can be enhanced by loading split-ring structures onto the SIWs. The CCRR is characterized by its electrically compact structure with a circular current pathway; the current flows along the ring structure to generate a magnetic field, which is represented as an inductance, while the openings of the ring and gaps between multiple rings represent capacitance. When the circuit is in a resonant state, this structure exhibits significantly elevated capacitance and inductance. Therefore, we designate the upper region of the CCRR as the measurement area, with dimensions of 10×10 mm.

A. Design Procedure

SIW is a new type of waveguide structure integrated on dielectric substrate. The TM_{nml} mode resonant frequency of the circular SIW is calculated by

$$f_{nml} = \frac{c}{2\pi \sqrt{\mu_r \varepsilon_r}} \sqrt{\left(\frac{P_{mn}}{a}\right)^2 + \left(\frac{\ell \pi}{d}\right)^2} \quad (3)$$

where ℓ is the number of half of the waveguide wavelength, a and d are the radius and height of the cavity, respectively, and P_{mn} is the m th root of the Bessel functions $J_n(x)$ of the first kind.

The proposed CCRR-SMSIW-type sensors are designed using an RO4350 dielectric substrate having relative permittivity $\varepsilon = 3.66$, $\tan \delta = 0.004$, and $h = 0.762$ mm. The transmission mode of the SMSIW resonator in the sensor is TM mode, with the fundamental mode being TM_{010} . According to formula (3), the resonant frequency TM_{010} of the fundamental mode is determined by

$$f_{\text{TM}_{010}}^{\text{SMSIW}} = \frac{2.405c}{2\pi R_{\text{eff}} \sqrt{\mu_r \varepsilon_r}} \quad (4)$$

where R_{eff} represents the equivalent radius of the SIW cavity, 2.405 is the first zero point of the Bessel function [12], c is the speed of light, ε_r is the relative permittivity of the substrate dielectric, and μ_r is the relative magnetic permeability of the substrate dielectric.

According to the working principle of the SIW [36], the electric field concentrated at the center of the fan-shaped SMSIW. Therefore, placing the CCRR resonant ring near the center maximizes the electric field radiation into the surrounding space, and the resulting sensor plane structure is shown in Fig. 2(a). As shown in Fig. 2(b), CCRR resonant ring radiation an extremely large electric field into the surrounding space, the maximum electric field at the CCRR resonant ring is 470 206 V/m, which significantly enhances the sensor's sensitivity. The CCRR structure is compact, with a circular current path. Electromagnetic simulation software (HFSS) was used to simulate the sensor and optimize its structure model. Fig. 2(c) shows the simulation of the resonant frequency of the sensor when the measured material is not loaded. In this setting, the resonant frequency is 5.75 GHz and the resonant depth is -21.45 dB.

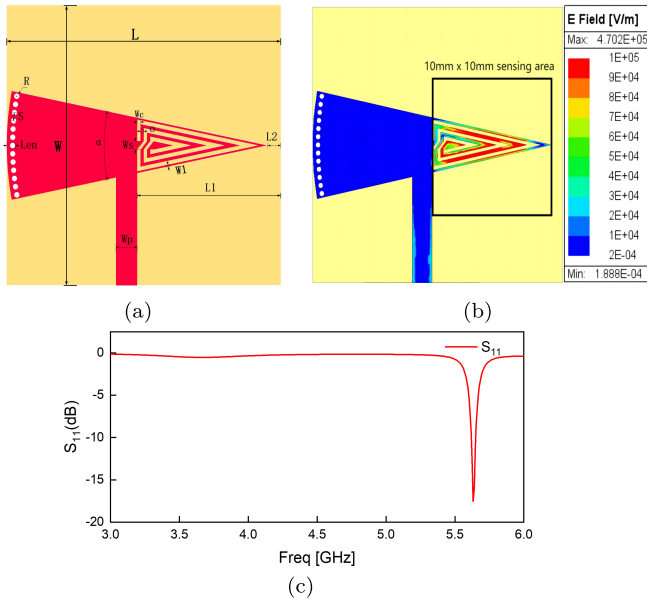


Fig. 2. (a) Planar structure of the CCRR-SMSIW sensor. (b) Electric field distribution map of the sensor. (c) Frequency response curve of CCRR-SMSIW.

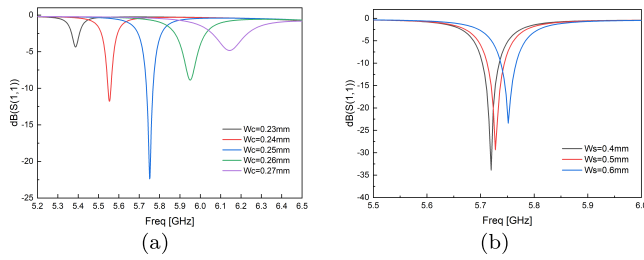


Fig. 3. (a) Effect of W_c on sensor performance. (b) Effect of W_s on sensor performance.

To study the influence of the groove width of CCRR resonant ring on the sensor performance, we conducted electromagnetic simulations on the CCRR groove width W_c , and the results are shown in Fig. 3(a). It can be seen from the simulation results that as W_c increases from 0.23 to 0.27 mm, the resonant frequency shifts to the right, and the resonance depth is the greatest at 0.25 mm. After several simulations of sensor sensitivity and various performance, it is found that the sensor has the best performance when W_c is 0.25 mm, so W_c is determined to be 0.25 mm. In addition, we also carried out a simulation study on the parameters of resonant ring opening W_s , and the simulation results are shown in Fig. 3(b). The simulation results show that when W_s of the sensor changes from 0.6 to 0.4 mm by a step of 0.1 mm, the resonant frequency shifts to the left. By optimizing other parameters, the final data in Fig. 2(a) are shown in Table I.

B. Equivalent Circuit Model

To ensure the accuracy of the design, we derived the equivalent circuit model of the sensor, as shown in Fig. 4(a). Equivalent circuit simulation and electromagnetic model simulation results are shown in Fig. 4(b). It can be seen that the circuit simulation results are basically consistent with

TABLE I
SIZE PARAMETER

Symbol	Size
L	21mm
W	20mm
α	$\pi/8$
Len	0.65mm
R	0.2mm
S	0.6mm
W_s	0.6mm
W_c	0.25mm
O	0.25mm
W_1	0.15mm
L_2	1mm
L_1	11mm
W_p	1.63mm

TABLE II
EQUIVALENT CIRCUIT PARAMETERS

Symbol	Value	Unit
C_q	3.80	pF
L_q	0.20	nH
C_s	5.52	pF
L_s	1.21	nH
C_r	0.14	nH
L_r	8.00	nH
L_d	9.35	nH
Z_0	50	Ω

the electromagnetic simulation results, and capacitors and inductors in equivalent circuits are ideal discrete device models that do not take into account actual losses. Therefore, at the resonant frequency, S_{11} curve is deeply indented. We regard the sensor model as left and right sectors, and then the left and right metallized holes are modeled as L_d , C_s and L_s represent the transmission of the left and right parts, C_r and L_r correspond to the conventional right-handed capacitance and inductance of SMSIW itself, C_q and L_q represent the influence between CCRR and SMSIW, Z_0 represents the impedance of the microstrip line, the width of the microstrip line is 1.63 mm, and $Z_0 = 50 \Omega$ is obtained through impedance calculation. The values of C_q and L_q will change when the MUT is loaded on the CCRR ring. This leads to a change in the resonant frequency of the sensor. The formula for calculating the resonant frequency of the sensor is

$$f = \frac{1}{2\pi\sqrt{C_q L_q}} \quad (5)$$

where f represents the resonant frequency with 5.75 GHz. After the simulation and optimization by Advanced Design System (ADS) software, the specific parameters of the circuit are shown in Table II.

C. Sensitivity Analysis

To obtain the sensitivity of the sensor, we observe the resonant frequency of the sensor in simulation on HFSS, by loading different sample materials with different permittivities. In the simulation, a sample material with dimensions of $10 \times 10 \times 0.762$ mm is loaded onto the resonant loop of

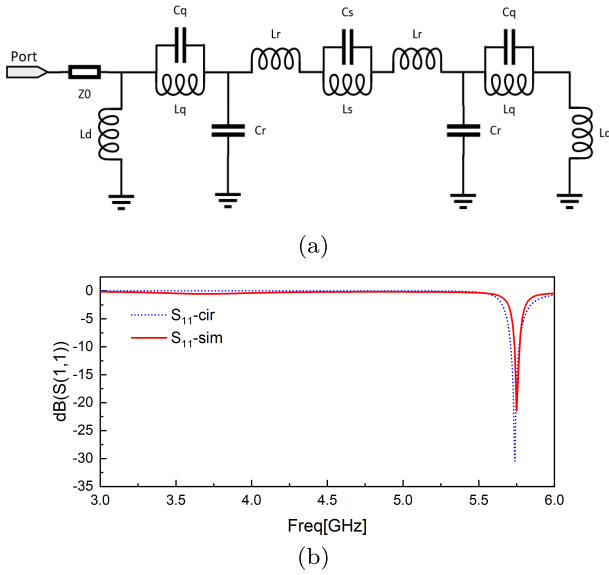


Fig. 4. (a) Equivalent model for CCRR-SMSIW. (b) Simulation results of the equivalent circuit model and electromagnetic model.

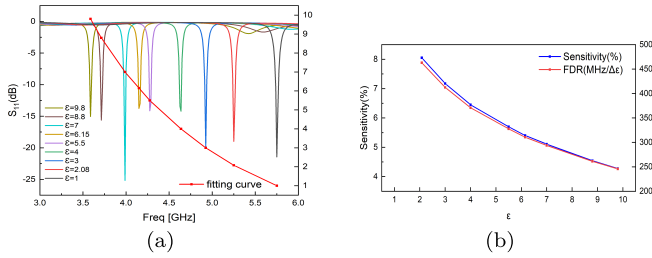


Fig. 5. (a) Electromagnetic simulation results of sensors and fitting curve. (b) Sensitivities and FDR.

the sensor's CCRR. The electromagnetic simulation results of sensors and the fitting curve are shown in Fig. 5(a). As the sensor transitions from a unloading state to a state loading a sample material with relative permittivity $\epsilon_r = 9.8$, the resonant frequency decreases with the increase in relative permittivity. The resonant frequency changes from 5.75 to 3.5875 GHz, with a frequency variation of 2.1625 GHz. Recording the values of resonant frequency when different relative permittivities are present, and using a polynomial curve fitting model to analyze the relationship between resonant frequency and relative permittivity. The mathematical model uses the least-squares method for curve-fitting, with the coefficient of determination 0.9999 ($R^2 = 0.9999$). The fitting function is shown in

$$\epsilon = -0.3748f^3 + 6.5568f^2 - 40.338f + 87.393 \quad (6)$$

where f is the resonant frequency of the sensor.

As described in [11] and [12], the equation for calculating the sensitivity of relative permittivity sensor is

$$S = \frac{|f_\epsilon - f_1|}{f_1} \times \frac{1}{\Delta\epsilon} \times 100\% \quad (7)$$

where f_ϵ is the resonant frequency when the sensor is loaded with a sample material with relative permittivity ϵ . f_1 is the resonant frequency when the sensor is unloaded. $\Delta\epsilon$ denotes

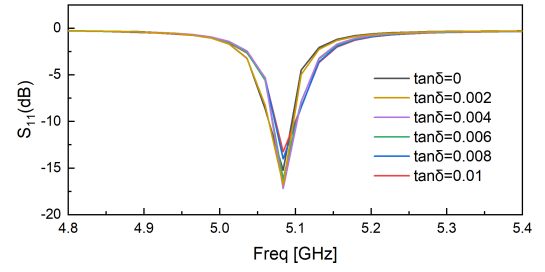


Fig. 6. Effect of different loss tangents on the resonant frequency.

the difference between the relative permittivities of the sample material and free space. Fig. 5(b) demonstrates the sensitivities and frequency detection resolution (FDR) when the sensor is loaded with different sample materials with different relative permittivities. The resolution of the sensor can be determined by FDR, as shown in

$$\text{FDR} = \frac{|f_\epsilon - f_1|}{\Delta\epsilon} \quad (8)$$

The sensitivity and resolution will monotonically decrease with the relative permittivity. It shows that our proposed sensor has high sensitivity and high resolution. The peak sensitivity and maximum resolution are 8.05% and 462.96 MHz/ $\Delta\epsilon$, respectively.

D. Other Parameter Analysis

Different materials under test not only have different permittivities but also the values of their loss tangent ($\tan \delta$) are different. The value of $\tan \delta$ of solid material reflects the relationship between the real and imaginary parts of permittivity. This relationship is described as

$$\tan \delta = \frac{j\epsilon'}{\epsilon} \quad (9)$$

where ϵ' is the imaginary part of permittivity and ϵ is the real part of permittivity. When the relative permittivity of the simulated test material is set to 2, different values of loss tangent are selected for simulation, and the simulation results are shown in Fig. 6. When the loss tangent value changes from 0 to 0.01 by a step of 0.002, the value of the resonant frequency does not change, so it can be shown that the loss tangent has no effect on permittivity measured by the sensor. To study the effect of MUT thickness on sensor performance, materials with the same permittivity but different thicknesses were selected for simulation. RO3006 with thicknesses 0.762 and 0.635 mm, respectively, were chosen for electromagnetic simulation. The simulation results are shown in Fig. 7(a). It can be seen that when the thickness is 0.762 and 0.635 mm, the resonant frequency of the sensor is 4.15 and 4.02 GHz, respectively. From formula (6), it can be seen that the measurement result of the permittivity is influenced on the frequency of the sensor, so the thickness of MUT will impact the permittivity measurement result. Within a certain range, the increase or decrease in the thickness of MUT will affect the accuracy of the measurement of the permittivity. In addition, we also studied the influence of MUT shape on the sensor, and we simulated the AD255C material

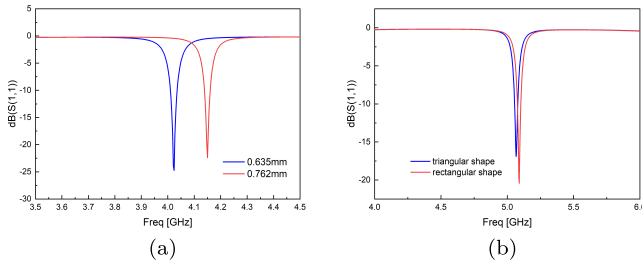


Fig. 7. (a) Effect of different thicknesses of MUT on resonant frequency. (b) Effect of different shapes of MUT on resonant frequency.

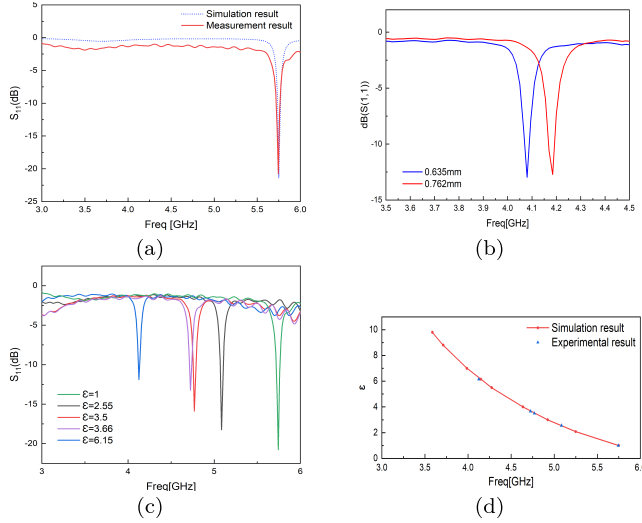


Fig. 8. (a) Comparison of measurement results with simulation results. (b) Measured results of RO3006 with two thicknesses. (c) Measurement results of four materials. (d) Comparison of experimental result with simulation result.

with a 10×10 mm rectangular shape and a triangle shape with a base of 6 mm and a height of 10 mm, which completely covered the CCRR structure. As shown in Fig. 7(b), sensor's resonant frequency is basically the same when triangle shape and rectangle shape MUT loaded on the sensor.

IV. MEASUREMENT AND DISCUSSION

Connecting the CCRR-SMSIW sensor to the VNA without loading MUT, we obtain the measured S_{11} curve which are compared with the simulation results from the electromagnetic simulation software HFSS. As shown in Fig. 8(a), the measurement results have slight discrepancies with the simulation results, with a resonant frequency of 5.745 GHz and an insertion loss of -20.78 dB. Due to manufacturing errors and parasitic parameters of the test device, there exists a certain deviation between the resonant frequencies in measurement and simulation. RO3006 materials with thicknesses of 0.762 and 0.635 mm, respectively, were used to verify the influence of MUT thickness on sensor test results. Two pieces of RO3006 with different thicknesses were placed above the CCRR resonant slot of the sensor, and clamps were used to ensure close contact between the MUT and the sensor, the experiment setup is shown in Fig. 9(a). Fig. 9(b) shows the physical photograph of the sensor and MUT. The test results are shown in Fig. 8(b). The test results indicate that when the

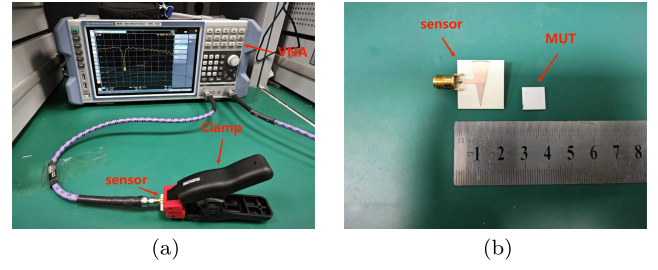


Fig. 9. (a) Experiment setup with LNA. (b) Physical photograph of the sensor.

thickness is 0.762 and 0.635 mm, the resonant frequency of the sensor is 4.18 and 4.08 GHz, respectively. The experimental results are basically consistent with the simulation results. The small error is caused by the manufacturing process error of the sensor and the surface flatness of the material. Four substrate materials with known different permittivities are selected as MUT. Permittivities of the samples are as follows: Rogers AD255C ($\epsilon = 2.55$), Taconic RF35 ($\epsilon = 3.5$), Rogers 4350 ($\epsilon = 3.66$), and Taconic RF60A ($\epsilon = 6.15$). These substrate materials have been applied widely in antenna design and microwave circuits. After many tests, we found that as long as CCRR is completely covered by MUT, the experimental results are almost unchanged. To cover the entire test area, the length and width of the samples are set to 10 and 10 mm, respectively. The thickness of all the four materials is uniformly set to 0.762 mm to ensure measurement consistency and eliminate the influence of thickness on the measurement results. The test results are shown in Fig. 8(c). We brought test results into the fitting curve, and it can be seen from Fig. 8(d) that the experimental results fit the simulation curve well. The equation for calculating the sensor error rate is expressed by

$$\text{Error}(\%) = \frac{|\epsilon_c - \epsilon_a|}{\epsilon_a} \times 100\% \quad (10)$$

where ϵ_a represents the actual relative permittivity and ϵ_c represents the relative permittivity calculated from (6). Table III shows the actual measurement results of the proposed sensor on four materials, in which f is the measured resonant frequency, Δf is the resonant frequency offset when different MUTs are loaded, ϵ_a is the actual permittivity of different MUTs, and ϵ_c is the permittivity of different MUTs measured by the proposed sensor. According to formulas (7), (8), and (10), the actual sensitivity, resolution, and error of the proposed sensor can be obtained. The results are shown in Table III, which are compared with that of the same type sensors. As shown in Table IV, the proposed sensor does not lose other performance while the sensor size is effectively reduced to $21 \times 20 \times 0.762$ mm. Compared with sensors of the same type, it has a higher sensitivity of 6.585% and a significantly high resolution of 378.46 MHz/ $\Delta\epsilon$. At the same time, it also has a very low error rate of 0.7845%. In addition, its MUT size is only $10 \times 10 \times 0.762$ mm, which is smaller compared with that of the same type sensors. These indicators fully confirm the superior performance of the proposed sensor, and in line with the development trend of sensor miniaturization. Therefore, the sensor can be effectively used to detect the permittivities of the materials.

TABLE III
DETAILED MEASUREMENT DATA FOR FOUR MATERIALS

Material	Rogers AD255C	Taconic RF35	Rogers 4350	Taconic RF60A
$f(\text{GHz})$	5.085	4.77	4.725	4.125
$\Delta f(\text{GHz})$	0.66	0.975	1.02	1.62
ε_a	2.55	3.5	3.66	6.15
ε_c	2.535	3.489	3.643	6.259
$S(\%)$	7.4	6.79	6.67	5.48
$FDR(\text{MHz}/\Delta\varepsilon)$	425.81	390	383.46	314.56
$Error(\%)$	0.588	0.314	0.464	1.772

TABLE IV
PERFORMANCE COMPARISON WITH SIMILAR SENSORS

Reference Type		Material Type	Frequency(GHz)	Sensitivity(%)	FDR(MHz/ $\Delta\epsilon$)	Error(%)	Size(mm)	MUT Size(mm)
[11]	CCRR-SIW	Solid	3.51	5.31	133	0.89%	52×34×0.508	15×15×1.52
[12]	CCRR-QMSIW	Solid	3.54	6.38	225.25	1.18%	26.5×26.5×0.762	10×10×0.762
[17]	CSRR-SIW	Solid	1.6,2.42	3.4,3.1	49.43,81.75	-	27.8×18.4×0.508	18.4×27.8×1.5
[34]	Triple-rings CSRR	Semi-Solid	2.5	4.806	-	-	25×20×1.52	-
[38]	CSRRs-SIW	Solid	8.64	-	102	less than 2%	-	27×4×3
[39]	SRR	Solid	2.48	4.61	114.3	0.63%	-	10×10
[40]	T-shaped	Solid	5.65	3.25	170	1.2675%	-	6.8×8.4
[41]	CSRs	Solid	3.086,3.248	1.45,1.4	162	2.482%	-	10×10
Proposed	CCRR-SMSIW	Solid	5.745	6.585	378.46	0.7845%	21×20×0.762	10×10×0.762

V. CONCLUSION

This article introduces a novel planar microwave sensor which incorporates a CCRR as a resonant component into an SMSIW. The CCRR is etched in the area of highest electric field concentration within the SMSIW cavity, which makes the sensor to measure permittivity of different solid materials efficiently. By simulation and measurement, the proposed sensor has high performance with an average sensitivity of 6.585%, an average resolution of 378.46 MHz/ $\Delta\varepsilon$, and a very low error rate of only 0.7845%. The capability can make the sensor highly suitable for a diverse range of applications spanning industries, agriculture, medicine, and beyond. Furthermore, our future research endeavors will delve into exploring the potential of this sensor configuration for liquid material characterization, with a focus on enhancing its performance and functionality in this regard.

REFERENCES

- [1] K. K. Singh, A. K. Singh, S. K. Mahto, R. Sinha, and A. J. A. Al-Gburi, "Enhanced accuracy and high sensitivity in dielectric characterization through a compact and miniaturized metamaterial inspired microwave sensor," *Sens. Actuators A, Phys.*, vol. 370, May 2024, Art. no. 115271.
- [2] X. Li, R. Singh, B. Zhang, S. Kumar, and G. Li, "S-tapered waveflex biosensor based on multimode fiber and seven-core fiber composite structure for detection of alpha-fetoprotein," *IEEE Sensors J.*, vol. 24, no. 4, pp. 4480–4487, Feb. 2024.
- [3] X. Liu et al., "SFFO cortisol biosensor: Highly sensitive S-flex fiber optic plasmonic biosensor for label-free cortisol detection," *IEEE Sensors J.*, vol. 24, no. 2, pp. 1494–1501, Jan. 2024.
- [4] A. K. Jha, A. Lamecki, M. Mrozowski, and M. Bozzi, "A microwave sensor with operating band selection to detect rotation and proximity in the rapid prototyping industry," *IEEE Trans. Ind. Electron.*, vol. 68, no. 1, pp. 683–693, Jan. 2021.
- [5] A. Ebrahimi, J. Scott, and K. Ghorbani, "Differential sensors using microstrip lines loaded with two split-ring resonators," *IEEE Sensors J.*, vol. 18, no. 14, pp. 5786–5793, Jul. 2018.
- [6] A. Ebrahimi, J. Scott, and K. Ghorbani, "Transmission lines terminated with LC resonators for differential permittivity sensing," *IEEE Microw. Wireless Compon. Lett.*, vol. 28, no. 12, pp. 1149–1151, Dec. 2018.
- [7] P. Vélez et al., "Portable reflective-mode phase-variation microwave sensor based on a rat-race coupler pair and gain/phase detector for dielectric characterization," *IEEE Sensors J.*, vol. 23, no. 6, pp. 5745–5756, Mar. 2023.
- [8] P. Vélez, F. Martín, R. Fernández-García, and I. Gil, "Embroidered textile frequency-splitting sensor based on stepped-impedance resonators," *IEEE Sensors J.*, vol. 22, no. 9, pp. 8596–8603, May 2022.
- [9] W.-J. Wu and W.-S. Zhao, "Microwave measurement system for characterizing liquid samples based on a modified HMSIW," *IEEE Sensors J.*, vol. 23, no. 19, pp. 22466–22475, Oct. 2023.
- [10] Y. Zhang, H. Shou, R. Liu, G. Ding, and Z. Mei, "A CSRR-based dual-peaks antenna sensor for full characterization of magneto-dielectric materials," *IEEE Sensors J.*, vol. 23, no. 21, pp. 25947–25957, Nov. 2023.
- [11] X. Han et al., "Microwave sensor loaded with complementary curved ring resonator for material permittivity detection," *IEEE Sensors J.*, vol. 22, no. 21, pp. 20456–20463, Nov. 2022.
- [12] T. Qi, G. Liu, J. Yu, and S. Jiang, "A quarter-mode substrate integrated waveguide microwave sensor loaded with CCRR for solid material measurement," *IEEE Sensors J.*, vol. 23, no. 18, pp. 21105–21112, Sep. 2023.
- [13] E. Díaz-Caballero, Á. Belenguer, H. Esteban, V. E. Boria, C. Bachiller, and J. V. Morro, "Analysis and design of passive microwave components in substrate integrated waveguide technology," in *IEEE MTT-S Int. Microw. Symp. Dig.*, Aug. 2015, pp. 1–3.
- [14] X. Wang, X. Zhu, C. Yu, and W. Hong, "Compact and low-phase-noise oscillator employing multilayer sixteenth-mode substrate-integrated waveguide filter for 5G applications," *IEEE Trans. Compon., Packag., Manuf. Technol.*, vol. 9, no. 9, pp. 1863–1871, Sep. 2019.
- [15] B. Scheiner et al., "Microstrip-to-waveguide transition in planar form using a substrate integrated waveguide," in *Proc. IEEE Radio Wireless Symp. (RWS)*, Jan. 2018, pp. 18–20.
- [16] F. Bilawal, F. Babaeian, K. T. Trinh, and N. C. Karmakar, "The art of substrate-integrated-waveguide power dividers," *IEEE Access*, vol. 11, pp. 9311–9325, 2023.
- [17] P. Mohammadi, H. Teimouri, A. Mohammadi, S. Demir, and A. Kara, "Dual band, miniaturized permittivity measurement sensor with negative-order SIW resonator," *IEEE Sensors J.*, vol. 21, no. 20, pp. 22695–22702, Oct. 2021.
- [18] H. Lobato-Morales, J. H. Choi, H. Lee, and J. L. Medina-Monroy, "Compact dielectric-permittivity sensors of liquid samples based on substrate-integrated-waveguide with negative-order-resonance," *IEEE Sensors J.*, vol. 19, no. 19, pp. 8694–8699, Oct. 2019.

- [19] K. H. El-Gendy, M. A. Khater, I. H. Abdelaziem, M. A. Abdalla, D. Peroulis, and M. F. Hagag, "Novel high-performance SIW cavity-based switching structures," *IEEE Trans. Microw. Theory Techn.*, vol. 72, no. 1, pp. 710–722, Jan. 2014.
- [20] Y. Chen, J. Huang, Y. Xiang, L. Fu, W. Gu, and Y. Wu, "A modified SIW re-entrant microfluidic microwave sensor for characterizing complex permittivity of liquids," *IEEE Sensors J.*, vol. 21, no. 13, pp. 14838–14846, Jul. 2021.
- [21] A. Belenguer, H. Esteban, and V. E. Boria, "Novel empty substrate integrated waveguide for high-performance microwave integrated circuits," *IEEE Trans. Microw. Theory Techn.*, vol. 62, no. 4, pp. 832–839, Apr. 2014.
- [22] Y. Shi, J. Liu, J. Lu, L. Qian, J. Zhou, and Z. Yu, "A new compact dual-band half-mode substrate integrated waveguide bandpass filter," in *Proc. Int. Conf. Microw. Millim. Wave Technol. (ICMMT)*, May 2023, pp. 1–3.
- [23] C. Fan, X. Liu, Z. Zhu, Y. Liu, and Y. Yang, "A compact quarter-mode (QM) and eighth-mode (EM) substrate integrated waveguide (SIW) filter," in *IEEE MTT-S Int. Microw. Symp. Dig.*, Nov. 2022, pp. 1–3.
- [24] G. J. Zhang, Y. Li, T. Chen, and Y. L. Song, "A compact quarter-mode SIW bandpass filter for 5G power IoT," in *Proc. Photon. Electromagn. Res. Symp. (PIERS)*, Nov. 2021, pp. 772–778.
- [25] Z. Akhter, M. A. Karimi, M. Arsalan, and A. Shamim, "Salinity-independent multiphase fraction metering for the oil and gas industry using microwave sensors," in *IEEE MTT-S Int. Microw. Symp. Dig.*, Jun. 2023, pp. 963–966.
- [26] S. Mukherjee, X. Shi, L. Udpa, S. Udpa, Y. Deng, and P. Chahal, "Design of a split-ring resonator sensor for near-field microwave imaging," *IEEE Sensors J.*, vol. 18, no. 17, pp. 7066–7076, Sep. 2018.
- [27] H. J. Peng et al., "A noncontact feed microwave metal devices deformation and stress sensor based on metamaterial," *IEEE Trans. Ind. Electron.*, vol. 70, no. 9, pp. 9642–9652, Sep. 2023.
- [28] A. K. Horestani, Z. Shaterian, and M. Mrozowski, "A compact and lightweight microwave tilt sensor based on an SRR-loaded microstrip line," in *Proc. 24th Int. Microw. Radar Conf. (MIKON)*, Sep. 2022, pp. 1–3.
- [29] Z. Shaterian and M. Mrozowski, "A multifunctional microwave filter/sensor component using a split ring resonator loaded transmission line," *IEEE Microw. Wireless Technol. Lett.*, vol. 33, no. 2, pp. 220–223, Feb. 2023.
- [30] J. Yu, G. Liu, Z. Cheng, Y. Song, and M. You, "Design of OCSRR-based differential microwave sensor for microfluidic applications," *IEEE Sensors J.*, vol. 22, no. 22, pp. 21489–21497, Nov. 2022.
- [31] Y. Beria, G. S. Das, A. Buragohain, and B. B. Chamuah, "Highly sensitive miniaturized octagonal DS-CSRR sensor for permittivity measurement of liquid samples," *IEEE Trans. Instrum. Meas.*, vol. 72, pp. 1–9, 2023.
- [32] M. A. H. Ansari, A. K. Jha, and M. J. Akhtar, "Design and application of the CSRR-based planar sensor for noninvasive measurement of complex permittivity," *IEEE Sensors J.*, vol. 15, no. 12, pp. 7181–7189, Dec. 2015.
- [33] W.-J. Wu and G. Wang, "A modified AMC-based antenna sensor for contactless measurement of complex permittivity," *Measurement*, vol. 206, Jan. 2023, Art. no. 112261.
- [34] A. J. A. Al-Gburi, N. A. Rahman, Z. Zakaria, and M. Palandoken, "Detection of semi-solid materials utilizing triple-rings CSRR microwave sensor," *Sensors*, vol. 23, no. 6, p. 3058, Mar. 2023. [Online]. Available: <https://www.mdpi.com/1424-8220/23/6/3058>
- [35] N. A. Rahman et al., "Liquid permittivity sensing using teeth gear-circular substrate integrated waveguide," *IEEE Sensors J.*, vol. 22, no. 12, pp. 11690–11697, Jun. 2022.
- [36] S. Akkader, H. Bouyghf, and A. Baghdad, "Miniaturization trends in substrate integrated waveguide for microwave communication systems," in *Proc. 2nd Int. Conf. Innov. Res. Appl. Sci., Eng. Technol. (IRASET)*, Mar. 2022, pp. 1–4.
- [37] L.-C. Fan and W.-S. Zhao, "A substrate integrated waveguide based sensor for fully characterizing magnetodielectric materials," in *Proc. Int. Conf. Microw. Millim. Wave Technol. (ICMMT)*, Sep. 2020, pp. 1–3.
- [38] H. Hao, D. Wang, and Z. Wang, "Design of substrate-integrated waveguide loading multiple complementary open resonant rings (CSRRs) for dielectric constant measurement," *Sensors*, vol. 20, no. 3, p. 857, Feb. 2020. [Online]. Available: <https://www.mdpi.com/1424-8220/20/3/857>
- [39] Q. Liu, H. Deng, P. Meng, and H. Sun, "High sensitivity sensor loaded with octagonal spiral resonators for retrieval of solid material permittivity," *IEEE Sensors J.*, vol. 21, no. 18, pp. 20010–20017, Sep. 2021.
- [40] S. Kiani, P. Rezaei, M. Navaei, and M. S. Abrishamian, "Microwave sensor for detection of solid material permittivity in single/multilayer samples with high quality factor," *IEEE Sensors J.*, vol. 18, no. 24, pp. 9971–9977, Dec. 2018.
- [41] H. Sun, H. Deng, P. Meng, S. Wang, Y. Shuai, and Q. Gao, "High-sensitivity sensor loaded with coupled complementary spiral resonators for simultaneous permittivity and thickness measurement of solid dielectric sheet," *IEEE Sensors J.*, vol. 22, no. 23, pp. 22591–22599, Dec. 2022.